*Article*

# Asymmetrical Multilevel Inverter-Based PV System with Voltage Feedback Control: An Experimental Validation

**Muhammad Najwan Hamidi** [1], **Arjuna Marzuki** [2,*], **Dahaman Ishak** [1], **Mohamed Salem** [1], **Mohd Hezri Marzaki** [2] and **Ikechi Augustine Ukaegbu** [3]

1   School of Electrical & Electronic Engineering, Universiti Sains Malaysia, Nibong Tebal 14300, Malaysia; najwan@usm.my (M.N.H.); dahaman@usm.my (D.I.); salemm@usm.my (M.S.)
2   School of Science and Technology, Wawasan Open University, George Town 10050, Malaysia; mdhezrimarzaki@wou.edu.my
3   Integrated Device Solutions and Nanophotonics Laboratory, School of Engineering and Digital Sciences, Nazarbayev University, Nur-Sultan 010000, Kazakhstan; ikechi.ukaegbu@nu.edu.kz
*   Correspondence: arjunam@wou.edu.my; Tel.: +60-12-6076420

**Abstract:** This paper presents an experimental evaluation and validation of a standalone photovoltaic (PV) renewable energy system using a perturb and observe MPPT-based voltage controller (POVC) for application on the reduced component multilevel inverter (MLI). The objective is to verify the effectiveness of POVC and asymmetrical MLI for real PV interconnection applications, which has never been reported before. An asymmetrical 17-level MLI topology is selected in this research. It requires four isolated DC sources to operate. A boost converter is deployed as one of the inputs while isolated DC power supplies power to the others. POVC is implemented at the boost converter to control the DC voltage from the PV panel. From the experimental results, the capability of the POVC to produce constant voltage levels under varying conditions is proven. It is also capable of delivering maximum power under maximum load. The full system is tested using different load types, including nonlinear loads. The MLI produces expected outputs under all operating conditions with efficiencies above 97%. The viability of the proposed PV system is firstly analysed through MATLAB/Simulink simulations. The results are then evaluated experimentally.

**Keywords:** multilevel inverter; asymmetric; PV system; voltage feedback control

## 1. Introduction

Because of its abundance in nature, solar photovoltaic (PV) energy is gradually becoming one of the most important renewable energy sources. It is pollution-free, requires less maintenance, and is less expensive to run [1]. In a standard PV renewable energy power system, the inverter and DC-DC converter are essential. The system can either be standalone or grid-connected [2,3]. The traditional two-level inverter is used in a lot of applications. However, due to limitations such as high harmonic content, reduced output resolution, high component stress, and lack of modularity, its applications are now limited to smaller-scale operations [4,5]. A multilevel inverter (MLI) was later introduced as a better alternative, with which most of the mentioned demerits are solved [6]. However, traditional MLI topologies, such as neutral point clamped (NPC), flying capacitor (FC), and cascaded H-Bridge (CHB), have several drawbacks in common. The demand for a higher number of components is one of them [7]. If the number of required components can be reduced, the overall cost of a system can also be reduced.

As a result, MLI topologies with a reduced number of components have been widely published over the years. This newer generation of MLIs uses fewer components, such as switches, capacitors, DC sources, and gate drivers, while maintaining similar or better output characteristics than older MLIs. One of the earliest reduced-component MLIs is known as the multilevel DC-link inverter (MLDCL), which makes use of an H-Bridge as

a polarity generator [8]. It is one of the most popular methods of reducing the overall number of switches, but the switches on the bridge need to block a very high voltage that is equivalent to the maximum output voltage [9]. Some other topologies, such as the T-Type and E-Type, avoid using the H-Bridge to reduce the high total blocking voltage at the cost of a higher number of components [10,11]. An improvement to the standard H-Bridge known as the packed H-Bridge was proposed years later [12]. It requires two extra switches. However, with the interconnection with optimal basic units, as presented in [13], a good balance between the number of components and total blocking voltage was successfully achieved. MLI can also be categorised according to its DC source connection architecture, which has its own set of benefits and drawbacks. There are MLI that require multiple isolated DC sources, while others need only single or several shared DC sources with capacitors. For the latter group, capacitors are needed to provide different voltage levels to generate multilevel outputs. A capacitor voltage balancing control system will be needed for the proper operation, which is rather complex to perform [14]. MLIs with isolated DC sources normally do not have capacitors. In some applications, such as variable frequency drive, isolated inputs can be harder to control. In other applications, such as PV interconnection, where multiple PV modules can be implemented as separate sources, isolated MLI can be simpler to implement and more advantageous [15].

The market for standalone PV energy systems is still available, especially in countries with rural areas where is it is economically expensive to connect these areas to the utility grid [16]. The DC-DC converter is necessary for a PV system to control the output from PV panels before serving as the input to the inverter [17]. In a standalone system, it is crucial to ensure the voltage at the input of the inverter is constant; otherwise, the AC output will be unstable. However, the characteristics of PV panels depend greatly on solar irradiation and operating temperature [18]. The standard modulation index-based DC-link voltage control method used in traditional MLI is not suitable to be applied in newer MLI topologies since the range for modulation index control will be smaller as the number of output levels increases [19]. There is also very little literature discussing this matter, especially in a standalone PV system. In some literature, a standard proportional-integral (PI) controller is implemented for voltage regulation purposes, and some others use artificial intelligence (AI) to auto-tune the PI controller [20,21]. Apart from tuning difficulty under dynamic operating conditions, PI-based DC voltage controllers suffer from a narrow regulation range since they do not have active power tracking capability where voltage regulation is only performed based on instantaneous PV voltage operating points [22]. Constant voltage has also been achieved by adjusting the load value, which is not practical for real applications [23].

Another aspect to consider is the maximum power point tracking (MPPT). Since MPPT requires a DC-DC converter [24], it is impossible to control the same converter for both MPPT and voltage regulation. One method discussed is the use of cascaded converters in which one converter operates for MPPT and the other for regulation [25]. Controlling the modulation index at the inverter stage is also not recommended in modern MLI since it can result in incorrect output with missing levels [15]. Some literature did not consider the variation of irradiance and temperature [26]. The perturb and observe MPPT-based voltage controller (POVC), as given in [27], is a better technique to achieve both voltage regulation and MPPT in a standalone PV system since voltage regulation is performed based on targetted power. Thus, active tracking is possible. However, the paper does not include any experimental evaluation.

In this paper, the experimental analysis of the POVC is presented. The research is further extended by connecting a boost DC-DC converter stage to an MLI for a standalone PV power system in an effort to study their suitability to be implemented as an alternative power source in rural areas. The POVC is used to regulate the voltage at one of the inverter's inputs. Under full-load conditions, POVC is employed for MPPT. Because there is still a paucity of literature on the ability of reduced component MLI with a high number of output levels to be connected to renewable energy sources, the isolated sources type MLI

architecture presented in [13] is selected. The simulations are run on MATLAB/Simulink software, and experimental hardware is built to confirm the findings.

## 2. System Modelling

### 2.1. Multilevel Inverter

The MLI topology from [13] was chosen in the proposed system, as stated in Section 1. The topology's structure is shown in Figure 1. The packed H-Bridge unit was the central part of the topology, which consisted of six switches ($S_1$, $S_2$, $S_3$, $S_4$, $S_5$, and $S_6$). The basic units were located on the bridge's right and left sides. On one side, the basic unit was positioned in the opposite direction to the basic unit on the other side. Each basic unit contained two DC sources ($V_{1/2}$ and $V_{3/4}$) and two unidirectional switches ($S_{7/8}$ and $S_{9/10}$).
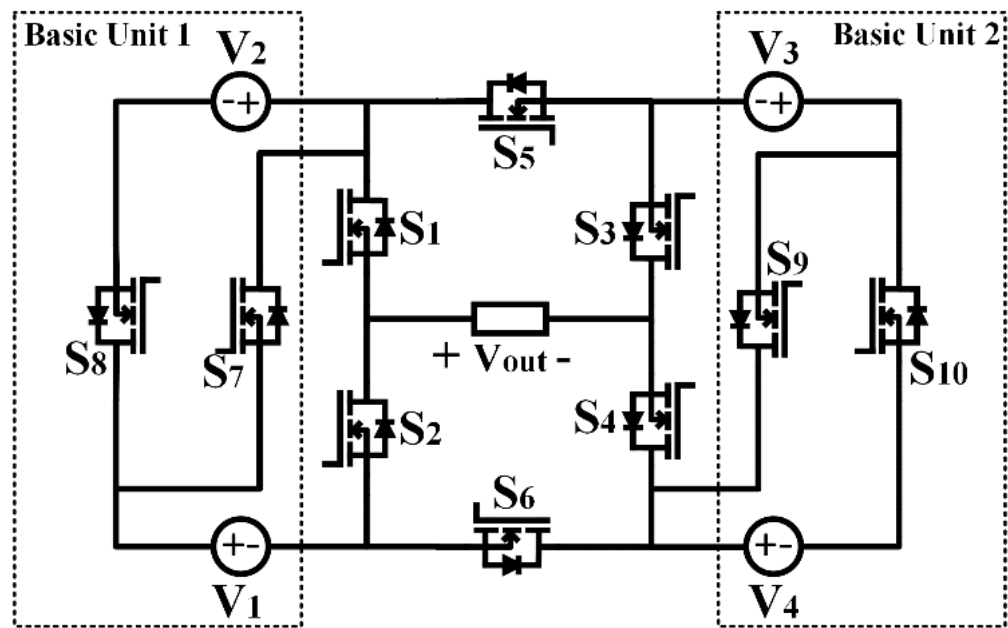


**Figure 1.** Selected MLI topology.

The topology could generate 17 output levels (17 L) using the configuration of asymmetrical sources. There were differences in the values of the DC sources in this arrangement. The DC sources ratio should follow $V_1 : V_2 : V_3 : V_4 = 1V_{DC} : 1V_{DC} : 3V_{DC} : 3V_{DC}$. Table 1 presents all the possible source combinations for generating the 17 L output. Although the topology could be cascaded into as many stages as needed, this paper only considered its 17 L operation.

**Table 1.** Voltage source combinations for 17 L operation.

| Levels | Combinations | Outputs |
|--------|--------------|---------|
| 1 | None | 0 |
| 2 & 3 | $\pm(V_1)$ | $\pm V_{DC}$ |
| 4 & 5 | $\pm(V_1 + V_2)$ | $\pm 2V_{DC}$ |
| 6 & 7 | $\pm(V_3)$ | $\pm 3V_{DC}$ |
| 8 & 9 | $\pm(V_1 + V_3)$ | $\pm 4V_{DC}$ |
| 10 & 11 | $\pm(V_1 + V_2 + V_3)$ | $\pm 5V_{DC}$ |
| 12 & 13 | $\pm(V_3 + V_4)$ | $\pm 6V_{DC}$ |
| 14 & 15 | $\pm(V_1 + V_3 + V_4)$ | $\pm 7V_{DC}$ |
| 16 & 17 | $\pm(V_1 + V_2 + V_3 + V_4)$ | $\pm 8V_{DC}$ |

## 2.2. Blocking Voltage and Maximum Current

The selected MLI topology had considerably lower total standing voltage (TSV) compared to conventional and a number of newer topologies. Because the blocking voltages across the switches in MLI were not similar, knowing only the TSV was generally inadequate. Understanding these voltages can assist in the selection of suitable device models during the design stage. First, the relationships for the blocking voltages at the central packed H-Bridge stage are given as follows:

$$VB_{s1} = VB_{s2} = 2V_{DC} \tag{1}$$

$$VB_{s3} = VB_{s4} = 6V_{DC} \tag{2}$$

$$VB_{s5} = VB_{s6} = 8V_{DC} \tag{3}$$

where $VB_{S1}$ to $VB_{S6}$ are the blocking voltages across the switches $S_1$ to $S_6$. As for the basic units on the left and right sides of the bridge, the equations for blocking voltages can be represented as follows:

$$VB_{s7} = VB_{s8} = V_{DC} \tag{4}$$

$$VB_{s9} = VB_{s10} = 3V_{DC} \tag{5}$$

where $VB_{S7}$ to $VB_{S8}$ and $VB_{S9}$ to $VB_{S10}$ are the blocking voltages across the switches $S_7$ to $S_8$ and $S_9$ to $S_{10,}$ respectively. From (1) to (5), switches $S_5$ and $S_6$ theoretically had the highest blocking voltages, while the lowest blocking voltages were across switches $S_7$ and $S_8$. With the presented equations, the TSV of the circuit was 40 $V_{DC}$. The maximum current flowing through every power switch, unlike the blocking voltage, was essentially the same as the maximum current produced at the load.

## 2.3. Source Power Sharing

Since the selected MLI requires four isolated DC inputs with asymmetrical magnitudes, the power required to be delivered by each of the inputs would also be different. The difference was also contributed to by the switching scheme of the topology, where the average conduction period by the sources was non-similar. In simple terms, the power provided by a DC source was the result of multiplying the source DC voltage by the average current flowing through it. By adding the product of current magnitudes and their corresponding conduction times over a half-period of output, including the zero levels, the average current could be obtained. As a result, by examining the width and magnitude of each current level, the average current flowing through each DC source can be given as:

$$I_{V1} = I_{C1} \cdot 100 \cdot \frac{V_{DC}}{Z} \cdot pf \tag{6}$$

$$I_{V2} = I_{C2} \cdot 100 \cdot \frac{V_{DC}}{Z} \cdot pf \tag{7}$$

$$I_{V3} = I_{C3} \cdot 100 \cdot \frac{V_{DC}}{Z} \cdot pf \tag{8}$$

$$I_{V4} = I_{C4} \cdot 100 \cdot \frac{V_{DC}}{Z} \cdot pf \tag{9}$$

where $I_{V1}$, $I_{V2}$, $I_{V3}$, and $I_{V4}$ are the average source currents, $I_{C1}$, $I_{C2}$, $I_{C3}$, and $I_{C3}$ are the summation of the product between the current magnitude and conduction period at every output level, Z is the load impedance, and pf is the power factor. Thus, each source's power delivered to the load can be calculated by multiplying the average current value by the magnitude of their respective DC source as follows:

$$P_{V1} = I_{V1}V_{DC} \tag{10}$$

$$P_{V2} = I_{V2}V_{DC} \tag{11}$$

$$P_{V3} = 3I_{V3}V_{DC} \tag{12}$$

$$P_{V4} = 3I_{V4}V_{DC} \tag{13}$$

where $P_{V1}$, $P_{V2}$, $P_{V3}$, and $P_{V4}$ are the power delivered by the sources. Finally, with the knowledge of the source power-sharing, the total input power, $P_{in}$ can be estimated using the following expression:

$$P_{in} = P_{V1} + P_{V2} + P_{V3} + P_{V4} \tag{14}$$

*2.4. System Overview*

The suggested PV renewable energy system had three primary stages, which were the PV module stage, DC-DC converter stage, and inverter stage. The inverter's output was directly linked to AC loads for standalone operation. The output rating of the inverter was set at 230 Vrms, 50 Hz. Figure 2 depicts the overview of the entire proposed system. The boost converter was only connected to one MLI input, while the other three inputs were powered by three independent DC power sources since the selected topology shown in Figure 1 had four isolated DC inputs; this was due to a scarcity of resources. For theoretical validation, this arrangement was fairly adequate since a similar concept would apply if the other sources were to be PV powered as well. The actual PV array was connected as the input to the boost converter, and POVC was deployed as the controller.
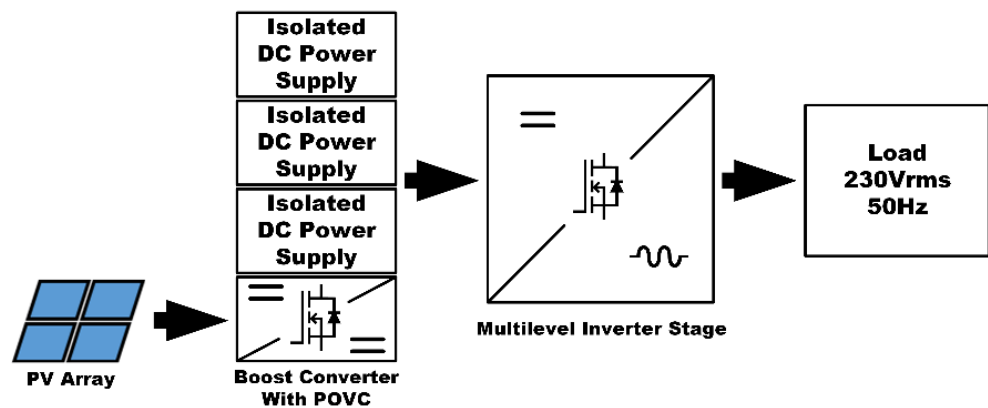


**Figure 2.** Overview of the proposed standalone PV system.

The POVC feedback controller was implemented to control the output voltage of the boost converter. The number of PV panels was selected based on the required power to be delivered by that particular source, based on Equations (10)–(13). A closer view of the implemented boost converter stage with POVC is illustrated in Figure 3.
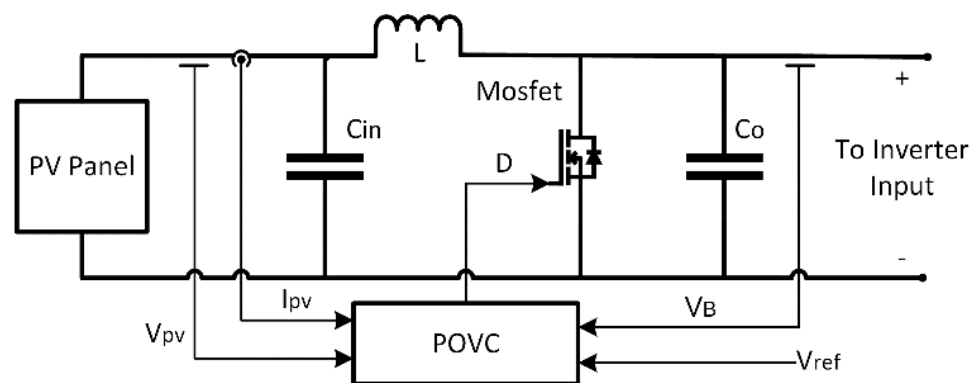


**Figure 3.** Boost DC-DC converter with POVC.

## 3. Control System

### 3.1. Perturb and Observe-Based Voltage Controller (POVC)

To ensure the DC voltage provided to the MLI by the boost converter was constant, POVC was deployed. This was necessary to ensure that the voltage generated by the inverter did not deviate from the specified value. Figure 4 shows a flowchart of the POVC operation.
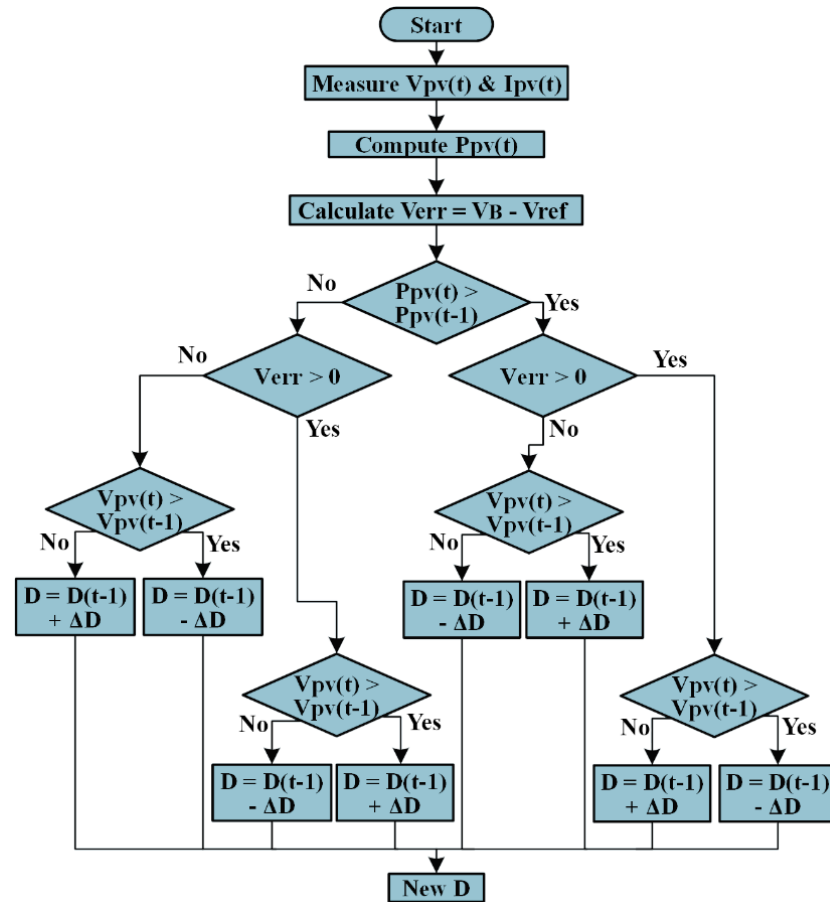


**Figure 4.** Flowchart of POVC.

The POVC was capable of producing constant DC voltages under varying solar irradiance, surrounding temperatures, and load levels. Its operation was principally similar to the original P&O MPPT algorithm. However, instead of tracking for maximum power point (MPP), the POVC would track for the targeted load power, $P_{Lref}$, by the addition of two duty cycle changing loops. The targeted load power $P_{Lref}$ was related to the reference voltage, $V_{ref}$, and load value, $X_L$, according to the following relationship:

$$P_{Lref} = \frac{V_{ref}^2}{X_L} \tag{15}$$

Power tracking, as in (15), was achieved by the algorithm of Figure 4 through the two added loops where $V_{err}$ was checked under different conditions of $P_{PV}$. Thus, at full-load, $V_{ref}$ would be equal to MPP voltage, $V_{MPP}$ at most, and $P_{Lref}$ would be equal to MPP power, $P_{MPP}$. With POVC, the PV operating point would be between $V_{PV} = 0$ and $V_{PV} = V_{MPP}$, which is the regulating range of the algorithm. This means that if the power required by any selected load fell within the range, the POVC would be able to maintain the desired

voltage. However, the operation was also dependent on the converter gain range according to the boost converter equation as follows:

$$V_B = \frac{V_{PV}}{1 - D} \text{ for } V_{PV} = 0 \text{ to } V_{MPP} \tag{16}$$

Referring to Figure 4, $V_{PV}$ is the PV voltage that determines the range of $V_B$ in (16). In the POVC operation, its minimum and maximum value were 0 and $V_{MPP}$, respectively. It is best to note that $V_{MPP}$ values vary based on solar irradiance and temperature. Thus, the range of $V_B$ in (16) is not fixed. A lower range could be expected at lower solar irradiances and vice versa. Based on (16), the range of $V_B$ was also affected by the duty cycle. An example of the voltage regulating range calculation is given in the Results. Figure 5 depicts the POVC regulating range and $P_{Lref}$ tracking operation. First, the POVC operated as a standard P&O MPPT algorithm to track for $P_{MPP}$ (P1) and continued operating at MPP (P2) until the boost converter voltage, $V_B$, equalled $V_{ref}$. As $V_{DC}$ was no longer increasing and fixed at a constant value, the POVC would then track $P_{Lref}$ (P3). Thus, the PV power should be maintained (by increasing PV current) to keep the PV operation at $P_{Lref}$ (P4).
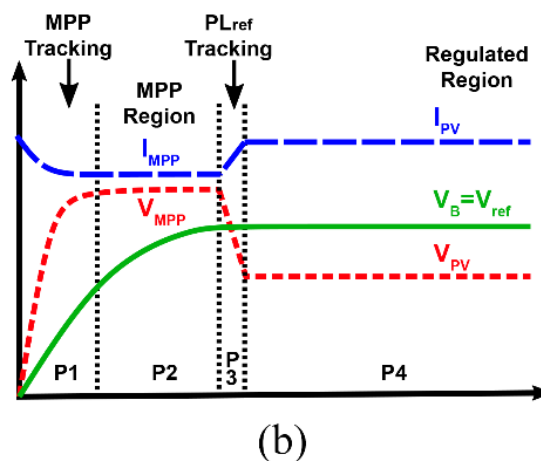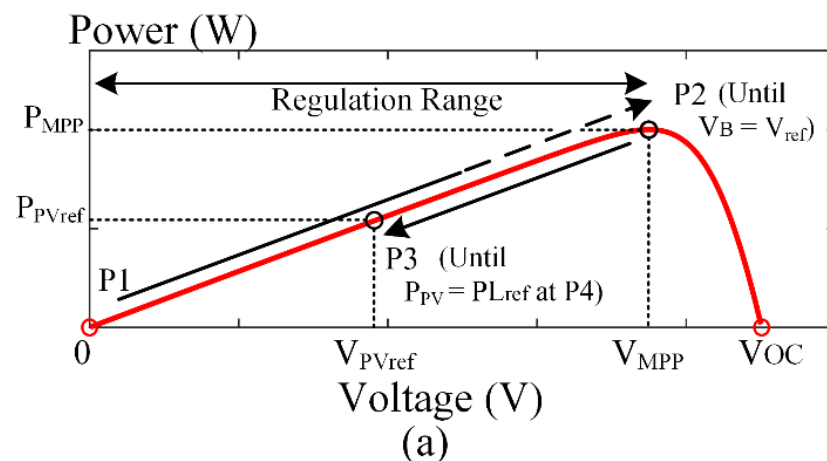


**Figure 5.** POVC tracking operation and regulating range representation using (**a**) P-V curve. (**b**) Input and output characteristics.

## 3.2. Controller Comparison

In this section, a brief theoretical comparison was conducted between the selected voltage control algorithm, which is the POVC, and several other voltage control techniques. The first technique compared was the cascaded converter method, where two different DC-DC converters are connected in series to allow both MPPT and voltage regulation ability [25,28]. The second technique was the inverter side control method, where voltage

regulation was achieved by modifying the modulation index of the pulse width modulation (PWM) at the inverter side switches [29–31]. The last selected voltage control technique was the PI-based controller, in which the PI controller was used to perform the voltage regulating operation by taking $V_{ref}$ and $V_B$ as the inputs to the controller [20–22]. The comparison is presented in Table 2. It can be concluded that the POVC had better characteristics overall compared to the other control methods for standalone PV applications where a very high voltage control range with power tracking ability could be achieved by using only a single controller and DC-DC converter.

**Table 2.** Voltage control technique comparison.

| Method | Regulation Range | Power Tracking | Number of Controllers | Comment |
|---|---|---|---|---|
| Cascaded DC-DC Converter [25,28] | High | Yes | 2 | Requires 2 DC-DC converters with separate controllers. |
| Inverter Side Control [29–31] | Low | No/Yes | 1/2 | Requires 2 controllers if power tracking is to be considered. Has lower regulating range at higher inverter output levels. |
| PI-Based Controller [20–22] | Low | No | 1 | Requires different tuning at different operating conditions. |
| POVC | High | Yes | 1 | Requires only a single controller for both power tracking and voltage regulation. |

### 3.3. Inverter Modulation

The modulation method used in this study is the same as that proposed in the original paper of the chosen MLI. It is a low-frequency modulation approach in which all of the switches' switching angles are computed beforehand. The method aims to produce an output that resembles a sinusoid as closely as possible, with each switching angle calculated in relation to a pure sinusoid according to the following simplified equations:

$$\theta_j = \sin^{-1}\left[\frac{1}{N_L - 1}(2j - 1)\right] \text{ for } j = 1, 2, \ldots \frac{N_L - 1}{2} \tag{17}$$

$$\theta_j = 180 - \sin^{-1}\left[\frac{1}{N_L - 1}(2j - 1)\right] \text{ for } j = \frac{N_L - 1}{2}, \ldots, 2, 1 \tag{18}$$

$$\theta_{N_L} = 180° \tag{19}$$

$$\theta_k = 360 - \theta_j \text{ for } j = N_L - 1, \ldots, 2, 1 \tag{20}$$

where $N_L$ is the number of MLI output levels, $\theta_j$ is the switching angle position up to $N_L - 1$, $\theta_k$ is the switching angle position from $N_L + 1$ up to $2N_L - 1$. The depiction of the expected 17 L output is displayed in Figure 6 using (17)–(20).
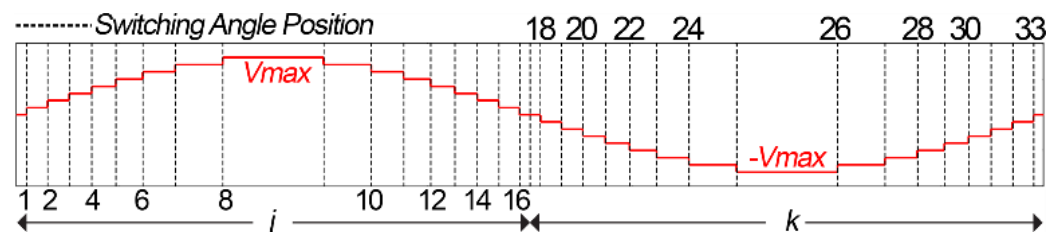


**Figure 6.** Switching angle positions.

## 4. Results and Discussion

A simulation study was first performed using Matlab/SIMULINK software to demonstrate the functionality of the entire system. To verify the simulation study and its findings, a hardware prototype was also developed. Various experiments were carried out on the POVC and its integration with the MLI using a boost DC-DC converter. The output characteristics of the 17 L MLI operation are likewise examined in this section. The experiment employed a solar panel with the specifications listed in Table 3 under standard operating conditions (STC). In the experiment, power MOSFET model GW30NC60KD was used for all switches. The experimental setup is depicted in Figure 7.

**Table 3.** PV panel characteristics at STC.

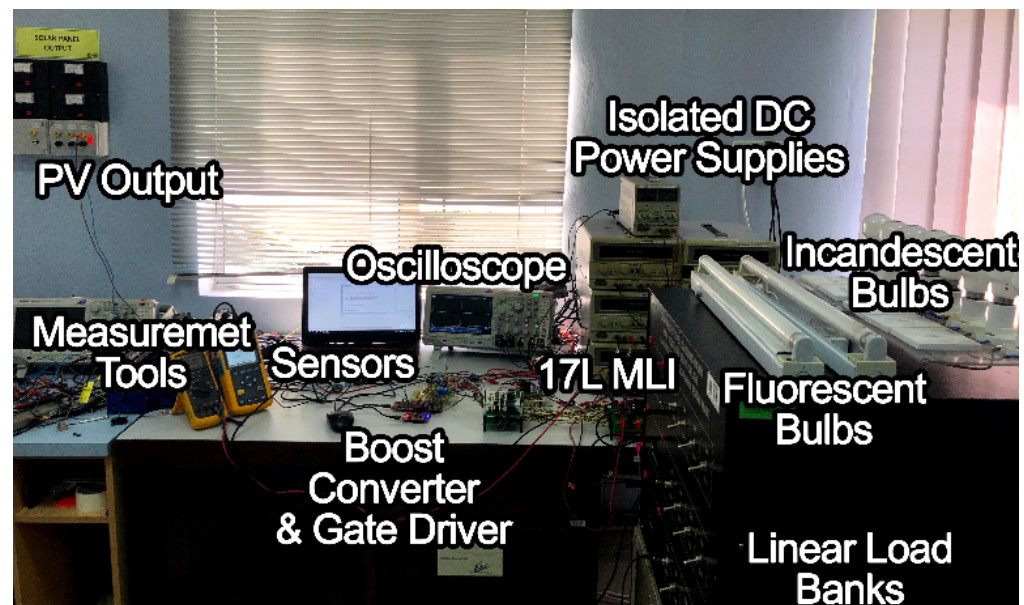| Parameters | Values |
|---|---|
| Power at MPP, $P_{mpp}$ (W) | 132.21 |
| Voltage at MPP, $V_{mpp}$ (V) | 26.39 |
| Current at MPP, $I_{mpp}$ (A) | 5.01 |
| Open Circuit Voltage, $V_{OC}$ (V) | 40.16 |
| Short-Circuit Current, $I_{SC}$ (A) | 5.614 |
| Temperature Coefficient of $V_{OC}$ (%/°C) | −0.35 |
| Temperature Coefficient of $I_{SC}$ (%/°C) | 0.05 |



**Figure 7.** Experimental setup.

### 4.1. POVC Test

To begin, independent POVC tests were performed without the boost converters connected to the MLI. One module of the PV panel with the specifications listed in Table 3 was linked to a single boost converter with a switching frequency of 20 kHz in the simulation. The temperature was maintained at a constant of 31 °C. With a fixed $V_{ref}$ of 40.66 V and a load of 58 Ω, the POVC was first evaluated for its reaction to rapid variations in irradiance; Figure 8 depicts the outcome. The value of 40.66 V was chosen since it is the value for $V_{DC}$, which will be addressed further in the upcoming section. The POVC successfully maintained the desired output voltage at all times, as shown in Figure 8.
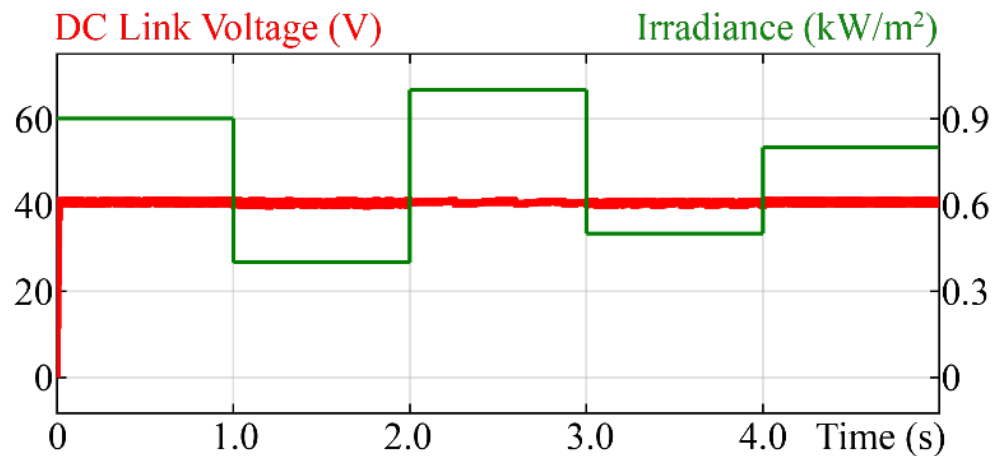
**Figure 8.** Boost converter voltage ($V_B$) vs. time under varying irradiances.

In the experimental analysis, since the actual PV module was used, it was impossible to adjust the irradiance and temperature manually, as in the simulation. Therefore, the POVC was tested at several different times of the day. At the irradiance of 838 W/m$^2$, temperature of 32 °C, and load of 58 Ω, the experimental results for voltage regulation, including all the measured values, is shown in Figure 9. A complementary simulation analysis to study the POVC start-up characteristic was conducted under the same environmental conditions to test the theory given in Figure 5. The simulation result is given in Figure 10. By comparing Figure 10 with Figure 5b, it can be seen that at the beginning of the operation, the POVC tracked MPP and stayed at the MPP region for a brief moment until $V_B$ reached the targetted $V_{ref}$. Afterwards, the system proceeded into the reference power tracking stage before finally reaching the steady-state operation at the targetted $V_B = V_{ref}$. Table 4 presents the voltage regulation experimental results obtained at several other tested irradiance levels.
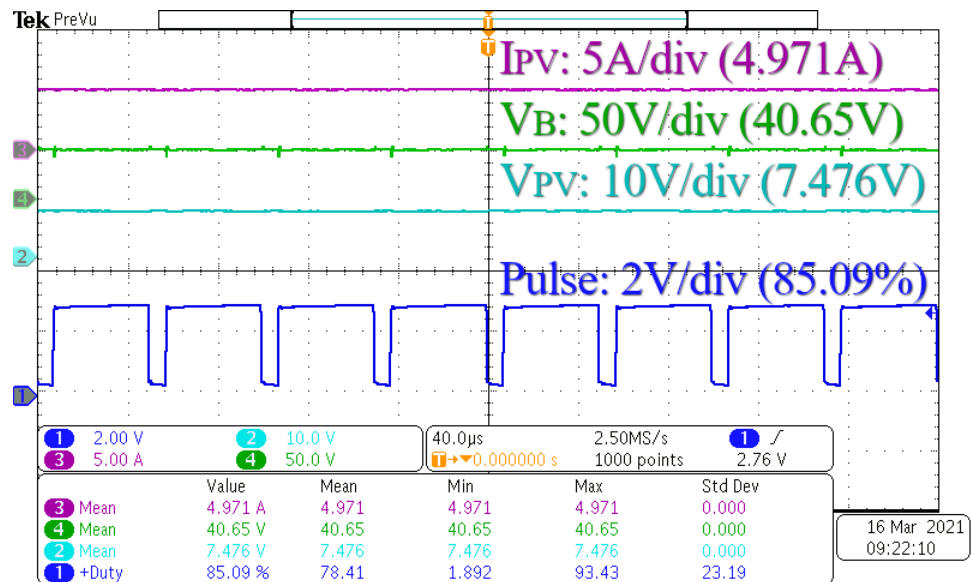


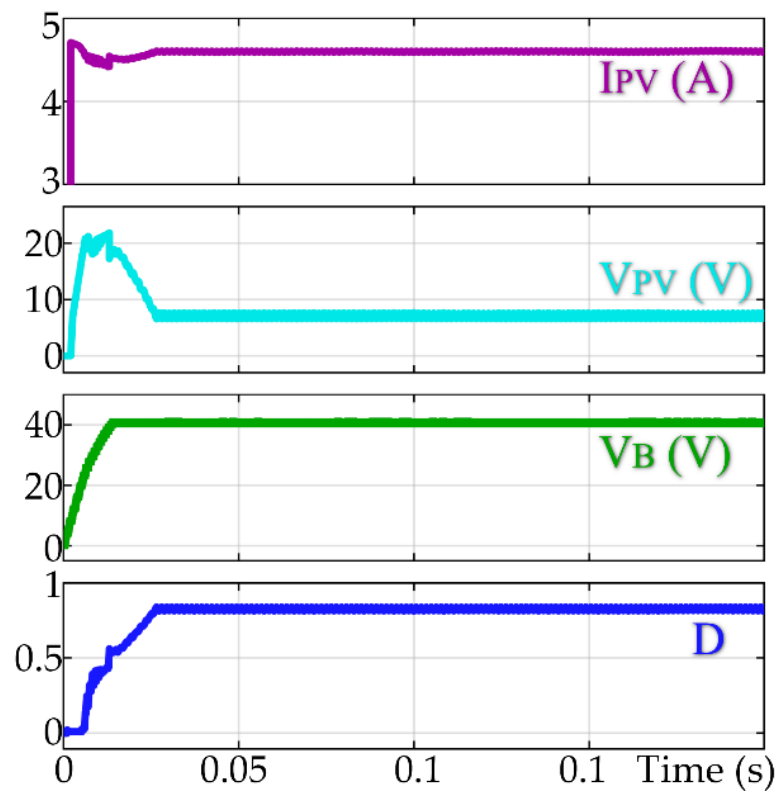**Figure 9.** Experimental voltage regulation at 838 W/m$^2$ and 32 °C.

**Figure 10.** Simulation voltage regulation at 838 W/m$^2$ and 32 °C.

**Table 4.** Experimental voltage regulation results at different irradiance levels.

| Irradiance-Temp (W/m$^2$–°C) | V$_{PV}$ (V) | I$_{PV}$ (A) | P$_{PV}$ (W) | V$_B$ (V) | Load (Ω) | P$_B$ (W) | Converter Efficiency (%) |
|---|---|---|---|---|---|---|---|
| 310–30 | 17.55 | 1.711 | 30.03 | 40.66 | 58 | 28.406 | 94.6 |
| 495–30 | 12.66 | 2.769 | 35.05 | 40.66 | 53 | 31.268 | 89.21 |
| 583–31 | 10.94 | 3.264 | 35.69 | 40.65 | 53 | 31.382 | 87.92 |
| 704–32 | 9.332 | 3.942 | 36.79 | 40.66 | 53 | 31.227 | 84.89 |

Next, the POVC was tested under the condition where the reference value was changed at several points during the operation. The irradiance and temperature were set at 582 W/m$^2$ and 31 °C, respectively. The selected environmental conditions and the moment they changed were based on the experimental results. The results obtained from both the simulation and experiment are shown in Figure 11. As can be observed, the experimental results were highly similar to the simulation findings, supporting that the proposed POVC was capable of accurately tracking all the specified reference values.

In terms of the voltage regulating range, as briefly described in Section 3.1, the voltage regulating range of the boost converter was not fixed and was directly affected by the solar irradiance and temperature. For instance, using the PV panel given in Table 3, at the irradiance of 800 W/m$^2$ and temperature of 31 °C, the theoretical maximum V$_B$ was 262.12 V if the maximum D was set at 0.9, according to (16). If the maximum allowable value of D was limited to 0.6, the maximum boost converter voltage was only 67.03 V. Differently; the theoretical minimum boost converter voltage would always be 0, regardless of environmental conditions.
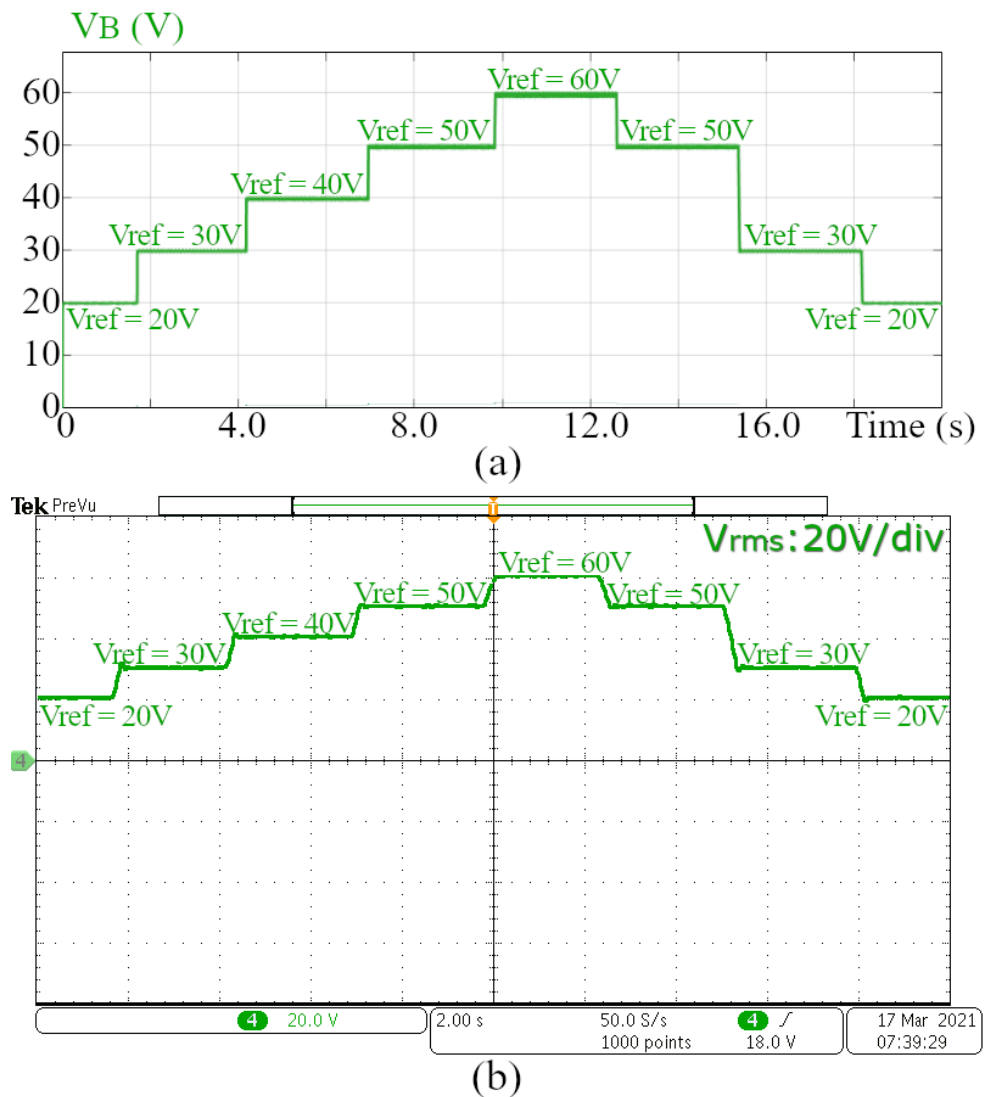
**Figure 11.** $V_B$ at varying irradiance levels from (**a**) simulation and (**b**) experiment.

*4.2. MPPT Test*

Lastly, the capability of the POVC to track the maximum power under full-load operation was studied. At the $V_{ref}$ value of 40.66 V, the MPPT results at several different irradiance levels are presented in Table 5. The temperature was fixed at the value of 31 °C. All the maximum load values were calculated based on the theoretical maximum power at every tested irradiance level. As shown in Table 5, decent MPPT ratios were obtained at all irradiance levels evaluated.

**Table 5.** Simulated MPPT test results at different irradiance levels.

| Irradiance (W/m$^2$) | Theoretical $P_{MPP}$ (W) | Maximum Load (Ω) | $V_{MPP}$ (V) | $I_{MPP}$ (A) | $P_{MPP}$ (W) | MPPT Ratio (%) | Converter Ratio (%) |
|---|---|---|---|---|---|---|---|
| 1000 | 128.1 | 12.91 | 24.75 | 5.093 | 125.7 | 98.13 | 97.45 |
| 800 | 108.9 | 15.18 | 25.97 | 4.140 | 107.3 | 98.53 | 97.39 |
| 600 | 86.35 | 19.15 | 27.29 | 3.137 | 85.6 | 99.10 | 97.28 |
| 400 | 60.36 | 27.39 | 28.74 | 2.094 | 60.2 | 99.73 | 96.89 |
| 200 | 31.11 | 53.14 | 29.64 | 1.049 | 31.1 | 99.94 | 95.01 |

Experimental replication of the prior simulation results was challenging to conduct because the maximum load value for any given set of environmental conditions should be determined. Since the irradiance and temperature are continually fluctuating, this is nearly impossible to ascertain. Furthermore, the maximum load is frequently very low, ranging from 10 $\Omega$ to 55 $\Omega$, and the load bank is incapable of producing such a required load. Thus, the POVC was operated as a normal P&O MPPT algorithm in the experimental test. This was achieved by setting the $V_{ref}$ to a very high value to force the POVC to track the maximum possible $V_{ref}$ value during any environmental condition. Therefore, output voltage regulation was not considered in these tests. P–V and I–V curves were used to illustrate the obtained MPPT experimental results, as shown in Figure 12. As can be seen, except at the two lowest irradiances, the POVR successfully brought the PV operating point very close to the actual MPP. It is also worth noting that the POVR's tracking zone extended from 0 V to $V_{MPP}$. This fact strongly relates to the theory presented in Section 3.
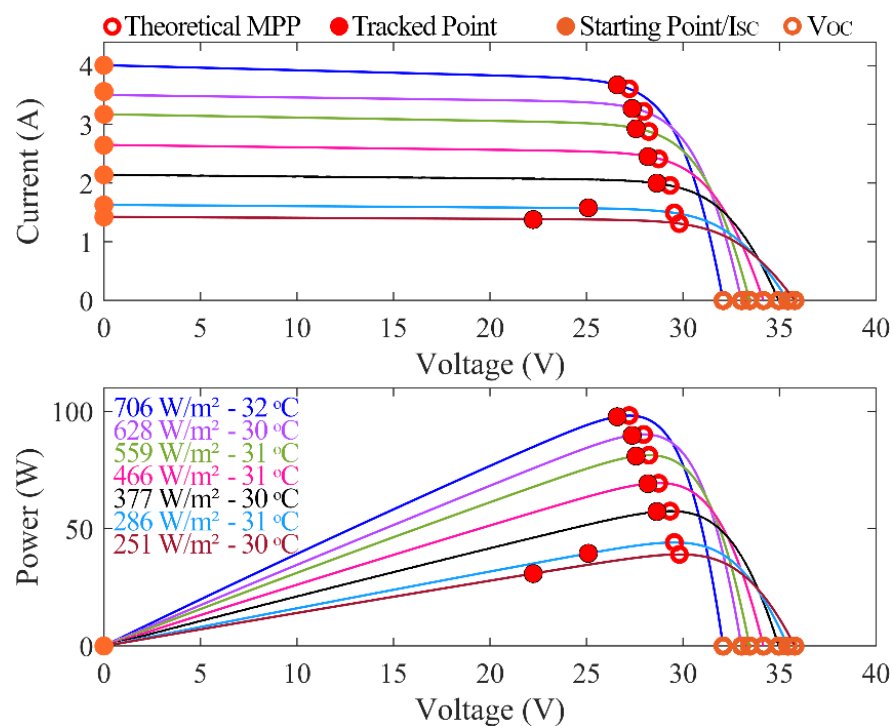


**Figure 12.** I–V and P–V curves of PV panel under the tested MPPT conditions. Efficiency analysis at RL = 258 $\Omega$, 0.44 H.

### 4.3. Full System Test

The full system tests were conducted based on the configuration depicted in Figure 2. All the generalised parameters used in both simulation and experimental studies of the full system are presented in Table 6. Due to the usage of an actual PV panel in the test, it was difficult to specify any constant environmental conditions throughout any single test because the irradiance and temperature change over time. As a result, tests were carried out as long as the PV panel produced sufficient power to meet the load demand at a given irradiance and temperature. The boost converter stage was connected to the input $V_2$ of the inverter. The $V_{ref}$ selected for the POVC operation is presented in the same table. All values were selected to achieve the output peak voltage of 325.27 V, which corresponds to 230 $V_{rms}$. Figure 13 presents the experimentally generated switching signals.

**Table 6.** Full system test parameters.

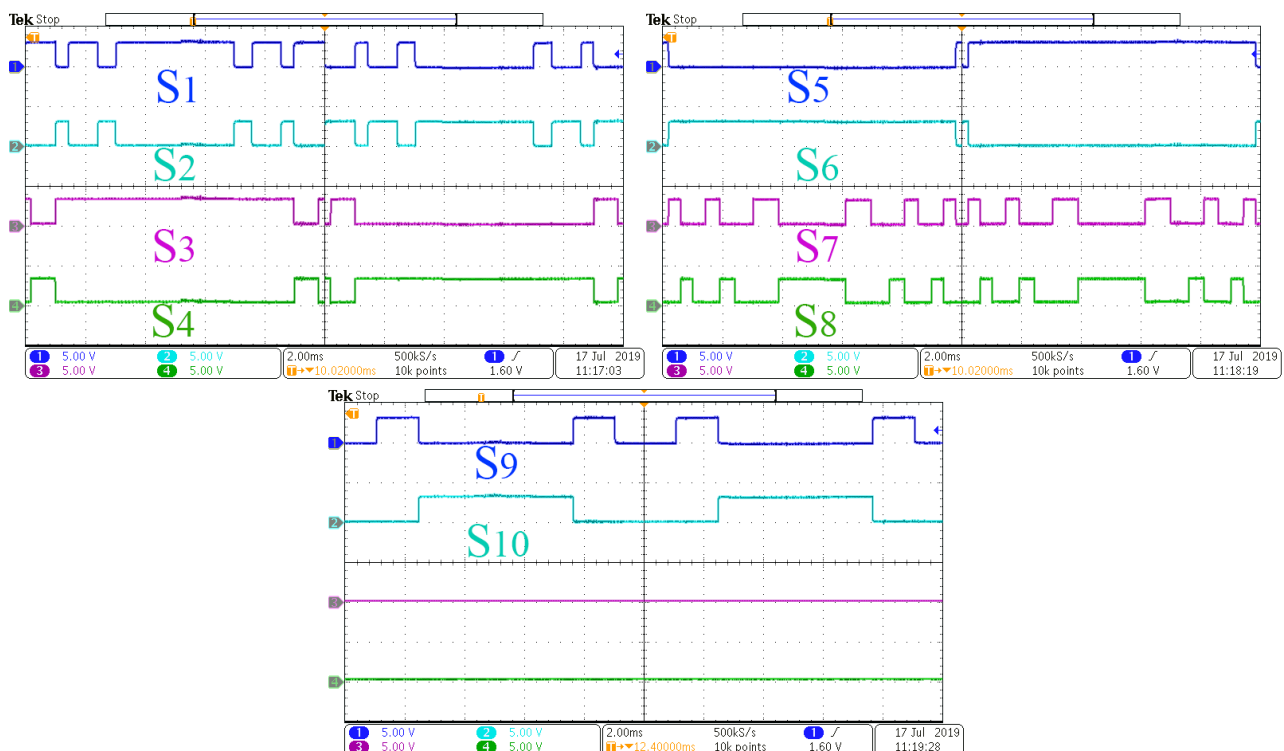| Parameters | Values |
| --- | --- |
| DC Power Supply $V_1$ ($V_{DC}$) | 40.66 V |
| POVC Reference Value for $V_2$ ($V_{DC}$) | 40.66 V |
| DC Power Supply $V_3$ ($3V_{DC}$) | 121.98 V |
| DC Power Supply $V_4$ ($3V_{DC}$) | 121.98 V |
| Output Voltage (Peak) | 325.28 V |
| Output Voltage (RMS) | 230 V |
| Output Frequency | 50 Hz |
| Boost Converters Switching Frequency | 20 kHz |



**Figure 13.** Experimental switching signals.

The operation of the system was tested under two types of loads, the purely resistive (R) load of 156 Ω and resistive-inductive load (RL) of 168 Ω, 0.33 H. All measurements were made after the input $V_2$ achieved its required voltage level from the boost converter. Figure 14 shows the voltage and current waveforms produced by the inverter from both simulation and experiment. Under the R load, both the voltage and current waveforms were observed to be perfectly in phase with identical patterns. They differed only in amplitude. This is due to the fact that a purely resistive load has no filtering effect, and its linearity causes the current to duplicate the voltage waveform in accordance with Ohm's law for every voltage step value and every voltage source combination. As a result, there was only active power present, which is entirely utilised by the load. The voltage and current waveforms were observed to be in phase with unity pf. Under the RL load, since the inductive component of the load acts as a low-pass RL filter, it could be seen that the current waveform was now smoothened and lagged the voltage waveform with the power factor pf of 0.86. The RL filter, in short, prevents high-frequency and allows low-frequency current signals to get through at the cut-off frequency, $f_{cut}$ which can be calculated using $R/2\pi L$. Any frequency greater than $f_{cut}$ was filtered, including high-frequency noise. For both

types of loads, the FFT analyses are given in Figure 15. Since the waveform shapes were identical, the output voltage and current under R load were found to have similar THD values of 3.87% from simulations. Experimentally, the voltage THD, THDv, and current THD, THDi values were also reasonably close. However, under the RL load, due to the inductive effect, the THDi has a reduced value of 0.38%, while the THDv still maintained an almost identical value of 3.88% as that obtained in the simulation. A similar case was also observed for the THDv measured experimentally. As for the experimental THDi, the value recorded by the power analyser meter was ~1.8%.
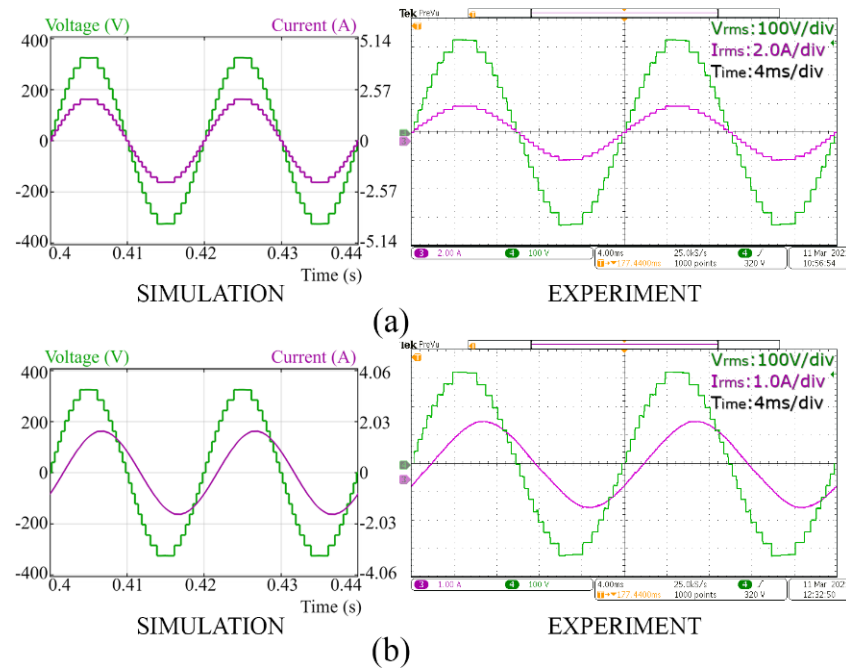


**Figure 14.** Output voltage and current waveforms obtained from simulation and experiment at the load of (**a**) R = 156 Ω, (**b**) RL = 168 Ω, 0.33 H.
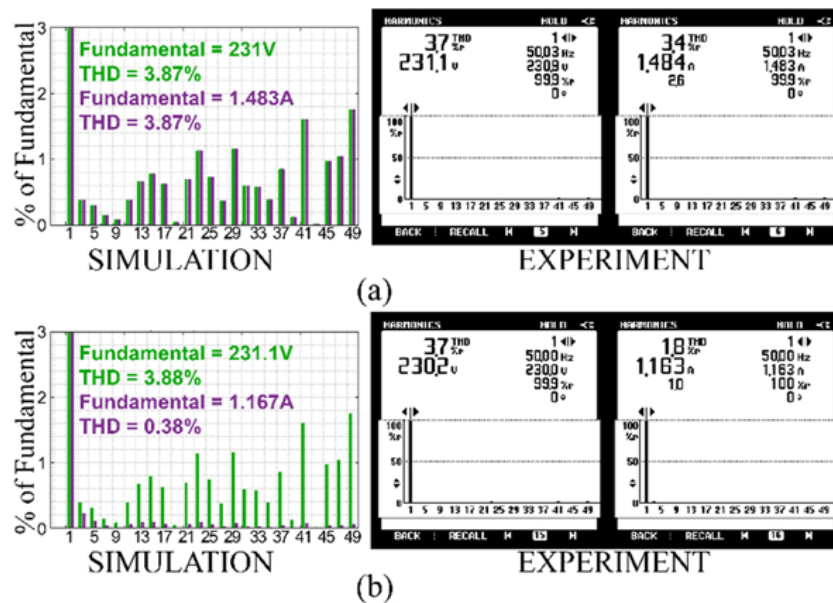


**Figure 15.** FFT analysis of voltage and current waveforms from simulation and experiment at the load of (**a**) R = 156 Ω, (**b**) RL = 168 Ω, 0.33 H.

### 4.4. Blocking Voltage Test

The relationships between the blocking voltages across the switches and the selected magnitudes of the DC sources were initially studied from simulation analysis. To verify the blocking voltage relationships in Section 2, the voltage across each switch was measured experimentally. With the $V_{DC}$ value of 40.66 V, as given in Table 6, the measured voltages across all switches are shown in Figure 16, where it can be concluded that all the measured maximum blocking voltages agree with the theoretical relationships given in Equations (1)–(5). The highest measured voltages were found across switches $S_5$ and $S_6$ with a value of ~325.28 V, which is equivalent to 8 $V_{DC}$. On the other hand, the blocking voltages across switches $S_7$ and $S_8$ were the lowest. They shared the same value of ~40.66 V, which was equivalent to $V_{DC}$. By summing up the blocking voltages, a net value of 1626.4 V was achieved, corresponding to ~40 $V_{DC}$, representing the TSV of the inverter.
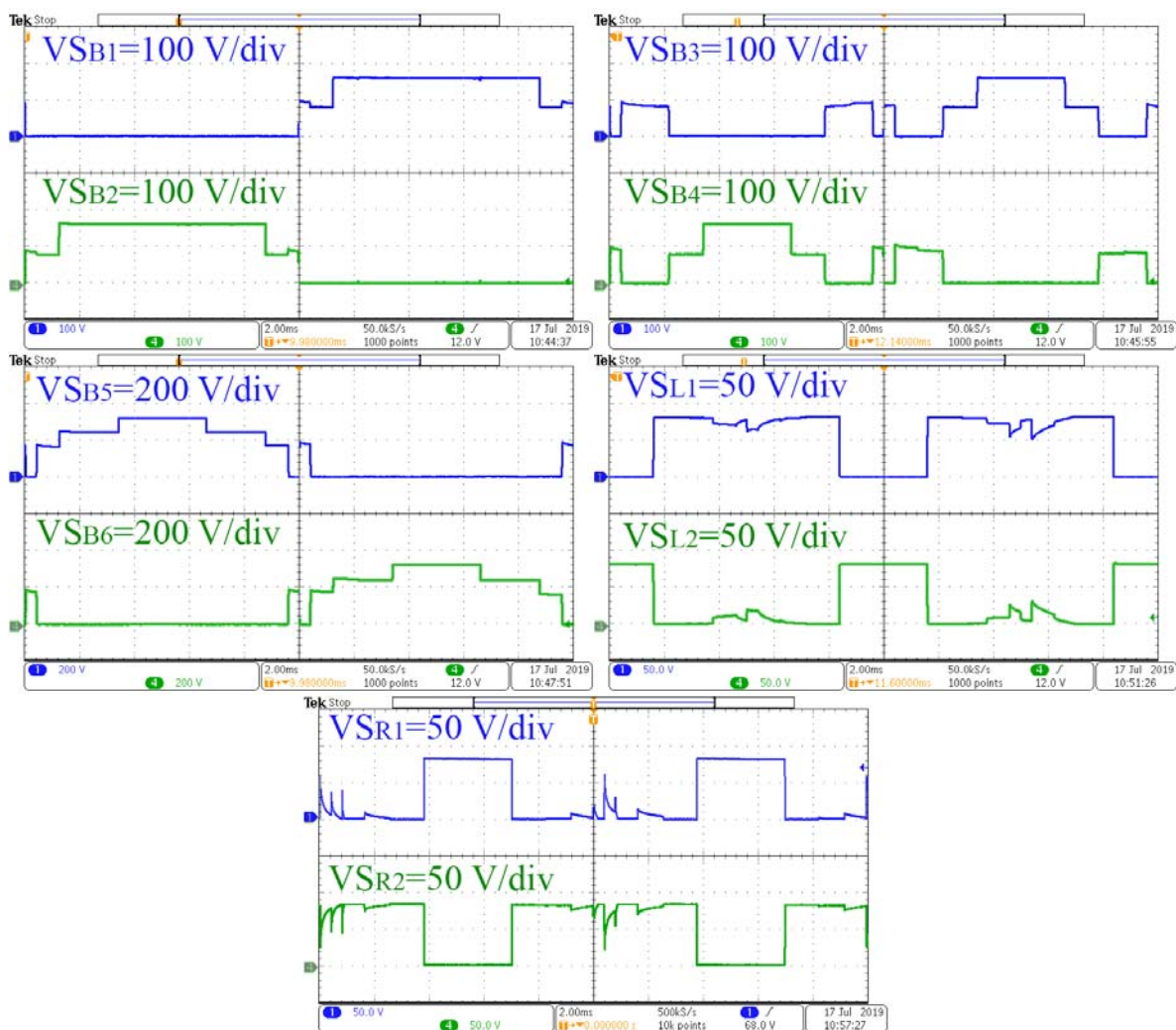


**Figure 16.** Experimentally measured blocking voltages across all switches.

### 4.5. Power Sharing and Efficiency

In this section, the complete system is tested again using different sets of R and RL load values. Then, the power shared by the DC sources is analysed along with the efficiency of the MLI. Presented in Tables 7 and 8 are the results obtained from the simulation study and experimental measurement. Based on the switching signals, referring to Equations (6)–(9),

the value for $I_{V1}$, $I_{V2}$, $I_{V3}$, and $I_{V4}$ were 41.24 m, 24.86 m, 48.64 m, and 37.27 m, respectively. With this, the power delivery ratio by the sources could be estimated as follows:

$$P_{V1} : P_{V2} : P_{V3} : P_{V4} = P_{V1} : 0.6028P_{V1} : 5.8701P_{V2} : 0.7662P_{V3} \qquad (21)$$

**Table 7.** Simulation (S) and experimental (E) tests of the full system with 17 L inverter under R load.

| Load (Ω) | Test | Source Power (W) | | | | $P_{in}$ (W) | $V_{inv}$ ($V_{rms}$) | pf | $P_{inv}$ (W) | THDv/i (%) | η (%) |
|---|---|---|---|---|---|---|---|---|---|---|---|
| | | $V_1$ | $V_2$ | $V_3$ | $V_4$ | | | | | | |
| 476 | S | 14.45 | 8.722 | 51.23 | 39.38 | 113.78 | 231.1 | 1.00 | 112.34 | 3.89/3.89 | 98.74 |
| | E | 15.10 | 8.692 | 51.40 | 39.45 | 114.65 | 230.1 | 1.00 | 111.37 | 3.7/3.2 | 97.14 |
| 156 | S | 43.87 | 26.45 | 155.4 | 119.1 | 344.86 | 231.0 | 1.00 | 342.57 | 3.87/3.87 | 99.34 |
| | E | 45.89 | 26.69 | 158.7 | 122.1 | 353.42 | 231.1 | 1.00 | 342.95 | 3.7/3.4 | 97.04 |
| 99 | S | 69.16 | 41.69 | 244.9 | 187.7 | 543.51 | 230.9 | 1.00 | 540.54 | 3.87/3.87 | 99.45 |
| | E | 68.77 | 43.61 | 247.4 | 190.8 | 550.59 | 229.7 | 1.00 | 534.97 | 3.6/3.2 | 97.16 |

**Table 8.** Simulation (S) and experimental (E) tests of the full system with 17 L inverter under RL loads.

| Load (Ω-H) | Test | Source Power (W) | | | | $P_{in}$ (W) | $V_{inv}$ (V) | pf | $P_{inv}$ (W) | THDv/i (%) | η (%) |
|---|---|---|---|---|---|---|---|---|---|---|---|
| | | $V_1$ | $V_2$ | $V_3$ | $V_4$ | | | | | | |
| 599–2.11 | S | 5.160 | 3.100 | 18.38 | 14.17 | 40.810 | 231.1 | 0.66 | 39.64 | 3.89/0.28 | 97.13 |
| | E | 5.290 | 3.030 | 18.53 | 14.02 | 40.880 | 231.3 | 0.66 | 39.84 | 3.5/0.8 | 97.46 |
| 168–0.33 | S | 29.66 | 17.77 | 105.2 | 80.59 | 233.21 | 231.1 | 0.86 | 231.94 | 3.88/0.38 | 99.45 |
| | E | 30.16 | 18.31 | 105.8 | 80.48 | 234.13 | 230.2 | 0.86 | 230.24 | 3.7/1.8 | 98.34 |
| 103–0.095 | S | 61.07 | 36.60 | 216.5 | 165.8 | 479.95 | 230.9 | 0.96 | 478.13 | 3.87/0.58 | 99.62 |
| | E | 61.97 | 38.75 | 220.7 | 170.1 | 491.50 | 230.5 | 0.96 | 476.64 | 3.7/1.2 | 96.98 |

From both tables, it can be noted that the source $V_2$ delivered only ~60% of the power provided by source $V_1$. Source $V_3$, on the other hand, offered ~590% of the total power produced by source $V_2$. Lastly, source $V_4$ was found to deliver only ~77% of the power distributed by source $V_3$. These experimental and simulated power-sharing results are very close to the theoretical ratios given in (21). The theoretical input powers under the three tested R loads were calculated to be 112.47 W, 343.17 W, and 540.75 W, respectively. As for the tested RL loads, the theoretical input powers were 39.73 W, 232.6 W, and 480.26 W, respectively. Again, these theoretical values were very comparable to the presented simulation and experimental results. The amount of power required for each source is generally based on the voltage magnitude and frequency at which they are switched ON to produce any voltage level. From the obtained power-sharing results, the amount of power each DC source stage needs to deliver is known. Therefore, the number of PV panels required per DC-DC converter stage can be estimated in the design process if all inputs are to be powered by the PV source. In terms of THD, they are all comparable in the case of R loads. For RL loads, THDv values remain consistent, while THDi values were reduced according to the pf value.

### 4.6. Real Load Test

In the last part of the experiment, the system was tested using real loads. The purpose was to verify the viability of the proposed system in real applications. Firstly, the output of the MLI was connected to incandescent light bulbs rated at 300 W. The output waveforms for both voltage and current are shown in Figure 17 with their respective FFT analysis. The behaviour of the incandescent bulb load was found to be very similar to that of the pure R load. This is because the incandescent bulb is nearly entirely resistive due to the

absence of external inductive or capacitive elements. There is still some reactance due to the construction of the bulb and its filament, but they are very insignificant. Thus, the voltage and current waveforms still produced comparable THD values.
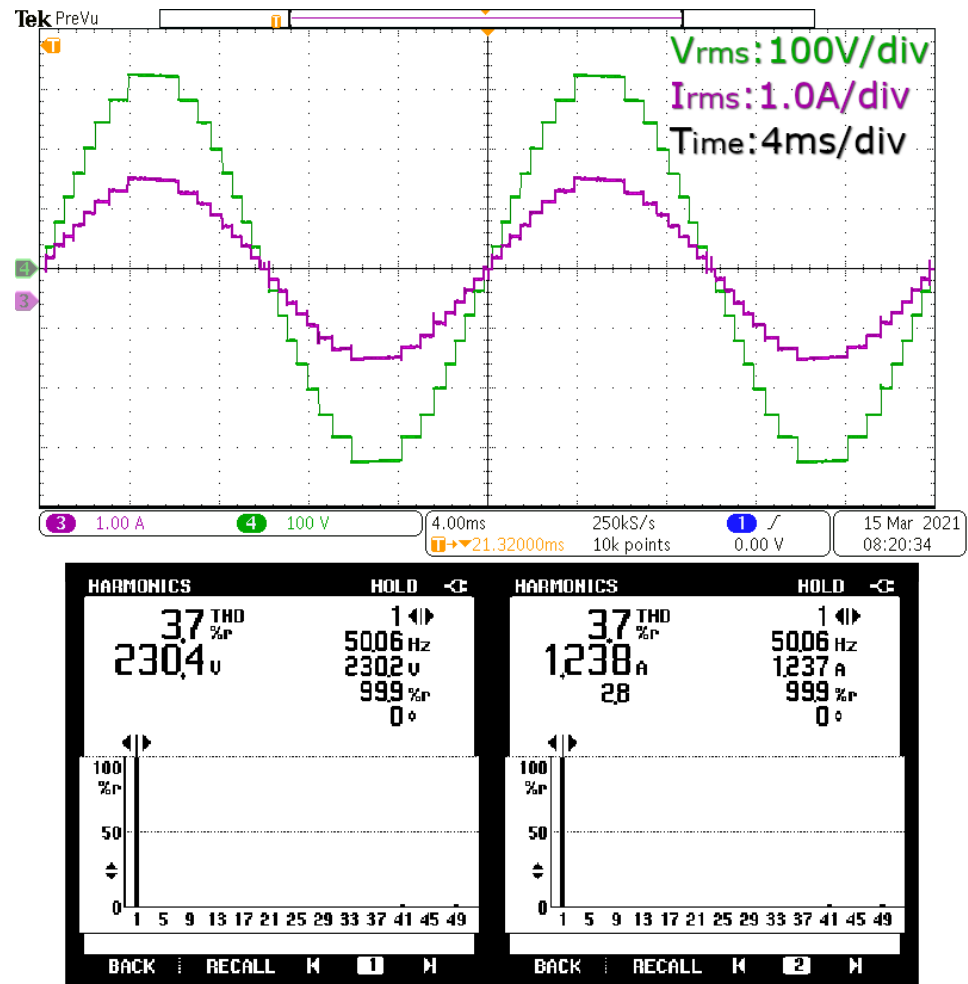


**Figure 17.** Experimental output waveforms and THD analysis under incandescent light bulb load.

The system was then tested using another type of real load, which is the fluorescent light bulb. Theoretically, fluorescent lights are nonlinear and are also very inductive due to the presence of magnetic ballast. The output voltage and current waveforms obtained using the fluorescent light load combination with the theoretical rated power of 120 W each are shown in Figure 18, along with their respective FFT analysis. As can be seen, the current did not have a pure sinusoidal waveform shape and appeared more triangular in shape even though its pf was very low. The pf, in this case, was 0.41 lagging. Furthermore, the voltage waveform was also seen to be slightly distorted. These phenomena were due to the characteristics of the fluorescent bulb load. In brief, because of the bulb's nonlinear nature, harmonic currents were generated, causing the current to be drawn in a non-sinusoidal pattern that is not proportionate to the voltage waveform. Despite a small deformation in its shape, the measured THDv value of 4.1% was only marginally higher than the previously reported values under linear R and RL loads. In contrast, THDi had the value of 6.9%, despite having a lower pf, due to its less-sinusoidal triangle waveform shape.
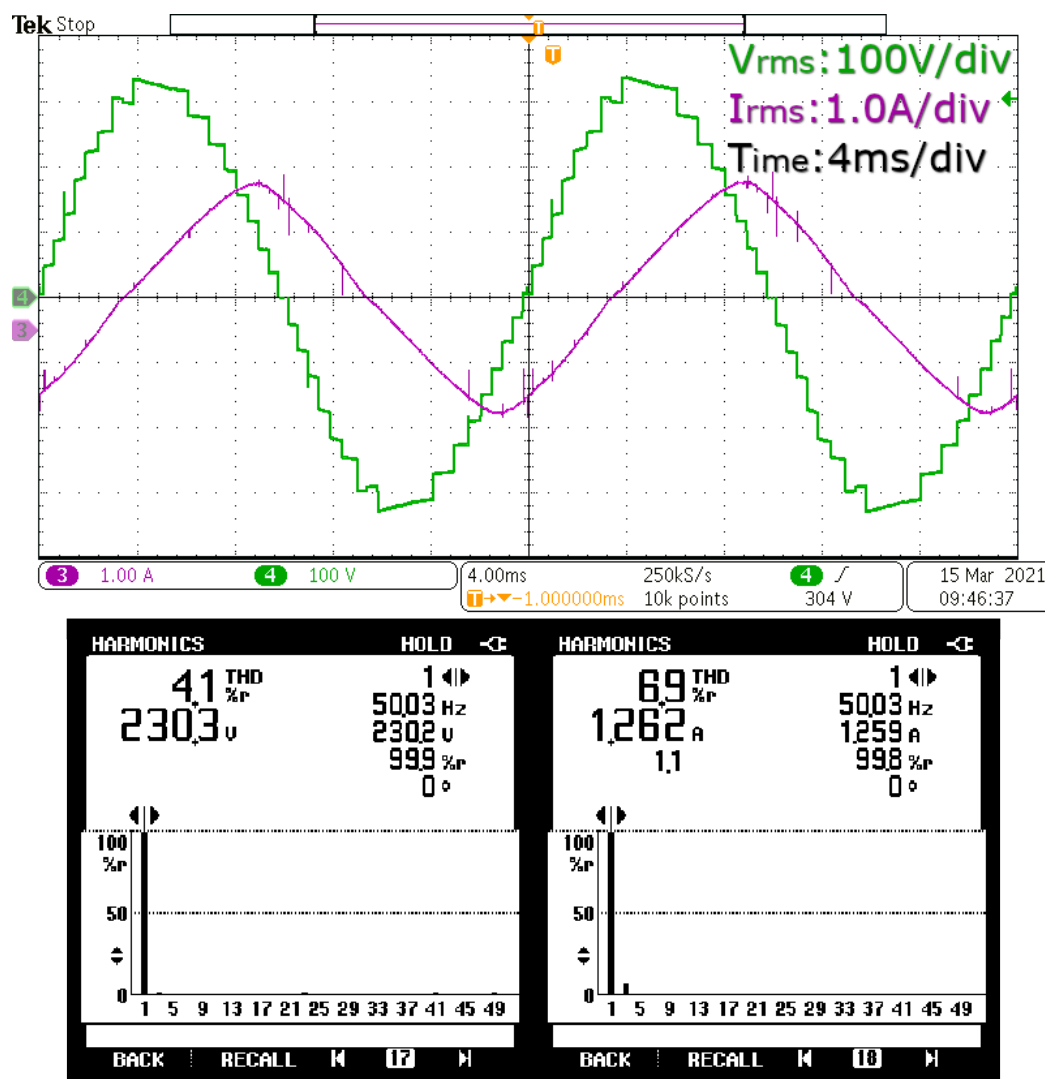
**Figure 18.** Experimental output waveforms and THD analysis under fluorescent light bulb load.

## 5. Conclusions

Experimental evaluation and validation of a standalone photovoltaic (PV) renewable energy system using perturb and observe MPPT-based voltage controller (POVC) for the application on the reduced component multilevel inverter (MLI) have been presented. The selected MLI was operated using its asymmetrical source configuration, which produces 17 output levels. Boost converters were used as one of the inputs of the MLI. POVC was deployed at the boost converter stage to regulate the output voltage before being fed to the input of MLI. From both simulation and experimental analyses, the POVC has demonstrated its ability to achieve voltage regulation under varying environmental and test conditions, including MPPT at full load. In the full system tests, 17 output levels were successfully generated at the targeted output rms voltage of 230 V. The power-sharing and blocking voltage test results obtained from both simulation and experiment were also very comparable. They were also close to the theoretical calculations. The system performed notably well with R, RL, incandescent light bulb, and fluorescent light bulb loads. From the results, the system was shown to be capable of powering up all the tested loads. The experimentally measured efficiencies were also very good, with the highest measured efficiency at 98.34% and the lowest at 97.03%.

## References

1. Dogga, R.; Pathak, M.K. Recent trends in solar PV inverter topologies. *Solar Energy* **2019**, *183*, 57–73. [CrossRef]
2. Sinha, A.; Chandra Jana, K.; Kumar Das, M. An inclusive review on different multi-level inverter topologies, their modulation and control strategies for a grid connected photo-voltaic system. *Solar Energy* **2018**, *170*, 633–657. [CrossRef]
3. Wang, L.; Wu, Q.; Tang, W. Energy Balance Control of a Cascaded Multilevel Inverter for Standalone Solar Photovoltaic Applications. *Energies* **2017**, *10*, 1805. [CrossRef]
4. Samadaei, E.; Kaviani, M.; Bertilsson, K. A 13-Levels Module (K-Type) With Two DC Sources for Multilevel Inverters. *IEEE Trans. Ind. Electron.* **2019**, *66*, 5186–5196. [CrossRef]
5. Mathew, K.; Mathew, J.; Azeez, N.A.; Dey, A.; Umanand, L.; Gopakumar, K. Multilevel dodecagonal space-vector generation for induction motor drives by cascading three-level and two-level inverters. *IET Pwr. Electr.* **2012**, *5*, 1324. [CrossRef]
6. Anas, M.; Sarwar, A.; Ahmad, A.; Alam, A.; Ahmad, S.; Sharaf, M.; Zaindin, M.; Firdausi, M. Generalized Structures for Switched-Capacitor Multilevel Inverter Topology for Energy Storage System Application. *Appl. Sci.* **2021**, *11*, 1319. [CrossRef]
7. Gupta, K.K.; Jain, S. Comprehensive review of a recently proposed multilevel inverter. *IET Power Electron.* **2014**, *7*, 467–479. [CrossRef]
8. Su, G.-J. Multilevel DC-Link Inverter. *IEEE Trans. Ind. Applicat.* **2005**, *41*, 848–854. [CrossRef]
9. Venkataramanaiah, J.; Suresh, Y.; Panda, A.K. A review on symmetric, asymmetric, hybrid and single DC sources based multilevel inverter topologies. *Renew. Sustain. Energy Rev.* **2017**, *76*, 788–812. [CrossRef]
10. Samadaei, E.; Sheikholeslami, A.; Gholamian, S.A.; Adabi, J. A Square T-Type (ST-Type) Module for Asymmetrical Multilevel Inverters. *IEEE Trans. Power Electron.* **2018**, *33*, 987–996. [CrossRef]
11. Samadaei, E.; Gholamian, S.A.; Sheikholeslami, A.; Adabi, J. An Envelope Type (E-Type) Module: Asymmetric Multilevel Inverters With Reduced Components. *IEEE Trans. Ind. Electron.* **2016**, *63*, 7148–7156. [CrossRef]
12. Mohd.Ali, J.S.; Krishnaswamy, V. An assessment of recent multilevel inverter topologies with reduced power electronics components for renewable applications. *Renew. Sustain. Energy Rev.* **2018**, *82*, 3379–3399. [CrossRef]
13. Hamidi, M.N.; Ishak, D.; Zainuri, M.A.A.M.; Ooi, C.A. Multilevel inverter with improved basic unit structure for symmetric and asymmetric source configuration. *IET Power Electron.* **2020**, *13*, 1445–1455. [CrossRef]
14. Filba-Martinez, A.; Busquets-Monge, S.; Bordonau, J. Modulation and Capacitor Voltage Balancing Control of Multilevel NPC Dual Active Bridge DC–DC Converters. *IEEE Trans. Ind. Electron.* **2020**, *67*, 2499–2510. [CrossRef]
15. Prabaharan, N.; Palanisamy, K. A comprehensive review on reduced switch multilevel inverter topologies, modulation techniques and applications. *Renew. Sustain. Energy Rev.* **2017**, *76*, 1248–1282. [CrossRef]
16. Al-Waeli, A.H.; Mahdi, H. Stand-alone PV systems for rural areas in Sabah, Malaysia: Review and case study application. *IJOCAAS* **2017**, *2*, 41–45. [CrossRef]
17. Dileep, G.; Singh, S.N. Selection of non-isolated DC-DC converters for solar photovoltaic system. *Renew. Sustain. Energy Rev.* **2017**, *76*, 1230–1247. [CrossRef]
18. Yang, Y.; Wen, H. Adaptive perturb and observe maximum power point tracking with current predictive and decoupled power control for grid-connected photovoltaic inverters. *J. Mod. Power Syst. Clean Energy* **2019**, *7*, 422–432. [CrossRef]
19. Jayapalan, G.; Edward, B. Design and Implementation of 15-Level Asymmetric Cascaded H Bridge Multilevel Inverter. *J. Electr. Eng.* **2018**, *17*, 396–404.
20. Anantwar, H.; Lakshmikantha, D.B.R.; Sundar, S. Fuzzy self tuning PI controller based inverter control for voltage regulation in off-grid hybrid power system. *Energy Procedia* **2017**, *117*, 409–416. [CrossRef]
21. Achiammal, B.; Kayalvizhi, D.R. Optimal tuning of pi controller using genetic algorithm for power electronic converter. *Int. J. Eng. Res.* **2013**, *2*, 6.
22. Hamidi, M.N.; Ishak, D.; Zainuri, M.A.A.M.; Ooi, C.A.; Tarmizi, T. Asymmetrical Multi-level DC-link Inverter for PV Energy System with Perturb and Observe Based Voltage Regulator and Capacitor Compensator. *J. Mod. Power Syst. Clean Energy* **2021**, *9*, 199–209. [CrossRef]
23. Sireesha, A. Generalized cascaded multi level inverter using reduced number of components with PV systems. In Proceedings of the 2016 Biennial International Conference on Power and Energy Systems: Towards Sustainable Energy (PESTSE), Bangalore, India, 21–23 January 2016; pp. 1–7.
24. Sarwar, S.; Javed, M.Y.; Jaffery, M.H.; Arshad, J.; Ur Rehman, A.; Shafiq, M.; Choi, J.-G. A novel hybrid MPPT technique to maximize power harvesting from pv system under partial and complex partial shading. *Appl. Sci.* **2022**, *12*, 587. [CrossRef]

25. Bhunia, M.; Gupta, R.; Subudhi, B. Cascaded DC-DC converter for a reliable standalone PV fed DC load. In Proceedings of the 2014 IEEE 6th India International Conference on Power Electronics (IICPE), Kurukshetra, India, 8–10 December 2014; pp. 1–6.

26. Mao, M.; Zhang, L.; Duan, Q.; Chong, B. Multilevel DC-link converter photovoltaic system with modified PSO based on maximum power point tracking. *Solar Energy* **2017**, *153*, 329–342. [CrossRef]

27. Hamidi, M.N.; Ishak, D.; Zainuri, M.A.A.M. Comparative evaluation of multilevel DC link inverter using symmetrical and asymmetrical DC sources. *J. Electr. Eng.* **2019**, *70*, 122–129. [CrossRef]

28. Ma, M.; Liu, X.; Lee, K.Y. Maximum Power point tracking and voltage regulation of two-stage grid-tied pv system based on model predictive control. *Energies* **2020**, *13*, 1304. [CrossRef]

29. Kumar, N.; Saha, T.K.; Dey, J. Sliding mode control, implementation and performance analysis of standalone PV fed dual inverter. *Solar Energy* **2017**, *155*, 1178–1187. [CrossRef]

30. Rezkallah, M.; Singh, S.; Chandra, A.; Singh, B.; Tremblay, M.; Saad, M.; Geng, H. Comprehensive controller implementation for wind-PV-diesel based standalone microgrid. *IEEE Trans. Ind. Appl.* **2019**, *55*, 5416–5428. [CrossRef]

31. Subramaniam, U.; Vavilapalli, S.; Padmanaban, S.; Blaabjerg, F.; Holm-Nielsen, J.B.; Almakhles, D. A Hybrid PV-battery system for ON-Grid and OFF-Grid applications—controller-in-loop simulation validation. *Energies* **2020**, *13*, 755. [CrossRef]